ARTICLE

Microstructural, Optical, and Electrical Properties of SnO Thin Films Prepared on Quartz via a Two-Step Method

Ling Yan Liang,[†] Zhi Min Liu,[†] Hong Tao Cao,[*,†] and Xiao Qin Pan[‡]

Division of Functional Materials and Nano Devices, Ningbo Institute of Material Technology and Engineering, Chinese Academy of Sciences, Ningbo 315201, People's Republic of China, and Department of Materials Science and Engineering, University of Michigan, Ann Arbor, Michigan 48109

ABSTRACT A simple, cost-effective, two-step method was proposed for preparing single-phase SnO polycrystalline thin films on quartz. X-ray diffraction (XRD) analysis demonstrated that the annealed films were consisted of polycrystalline α-SnO phase without preferred orientation, and chemical composition analysis of the single phase in nature was analyzed using X-ray photoelectron spectroscopy (XPS). Transmittance spectra in UV−vis−IR range indicated that the average transmittance of both the as-deposited and the annealed SnO thin films was up to 70%. The optical band gap decreased from 3.20 to 2.77 eV after the annealing process, which was attributed to the crystalline size related quantum size effect. Photoluminescence (PL) spectrum of the annealed film showed only a weak peak at 585 nm, and no intrinsic optical transition emission was observed. Moreover, the p-type conductivity of SnO film was confirmed through Hall effect measurement, with Hall mobility of 1.4 $cm^2\ V^{-1}\ s^{-1}$ and hole concentration of 2.8 × 10^{16} cm^{-3}.

KEYWORDS: tin oxide • quantum size effect • optical band gap • p-type conductivity • thin film transistor;

INTRODUCTION

Two stoichiometric tin oxide compounds, SnO and SnO_2, are known to be wide band gap oxide semiconductors with tetragonal litharge and rutile type structures, respectively (1). Of these, SnO_2 has been widely explored in applications of gas sensors, solar cells, transparent electrodes and thin film transistors (TFTs) (2−4). Nevertheless, in the past decades, SnO was the key material as anode material (5, 6), coating substance (7), catalyst (8), and precursor for the production of SnO_2 (9, 10), because of its properties of gas-sensitivity and metastability to transform into SnO_2 at O_2-rich ambient. Recently, SnO has been drawn back into attention simply because of the difficulty in obtaining high-quality p-type materials, including p-type doped ZnO (11), NiO (12), Cu_2O (13), etc. Compared to those materials, SnO could be a better native p-type oxide semiconductor because of Sn 5s nature at the valence band maxima (VBM), which might result in a more effective hole transport path and higher hole mobility (14, 15). In fact, previous studies show that the maximum hole mobility of SnO films is about 2.6 $cm^2\ V^{-1}\ s^{-1}$, fairly high among p-type conductive oxides, and it can be further improved via proper doping (16). Those properties endow SnO a promising candidate to be a next p-type oxide semiconductor utilized for novel optoelectronic and electronic devices. Especially, the fabrication of p-channel TFTs based on epitaxial SnO films, marks the beginning of SnO's application in complementary inverters and more complicated logic circuits (14, 17).

Device application requires the control of the chemical composition and microstructure which determine the optical and electrical properties of film. Even though epitaxial SnO film has been obtained, the conditions of expensive substrates (like single-crystalline yttria-stabilized zirconia and α-sapphire), and narrow growth window confine the commercial applications. In addition, the microstructure and composition of the films are affected by substrate through the lattice mismatch and thermal expansion coefficient mismatch (18). As a consequence, the optical band gap of SnO is reported to be scattered in a wide range, i.e., 2.5−3.4 eV (1, 14, 15). This variation in band gap was believed to be closely associated with the structural defect and impurity phase, or more concretely with the existence of SnO_2 (19−21). However, no unambiguous evidence has been given so far for those assertions. Therefore, there is a need for further study of the optical properties of SnO films with respect to their microstructure, chemical composition, etc.

Several techniques have been adopted in the growth of SnO films on various substrates, including reactive rf magnetron sputtering (22), e-beam evaporation (11), laser ablation (9, 14), atomic layer deposition (5), etc. However, the prepared SnO films are often mixed with some impurity phases, including metallic β-Sn, SnO_2, and intermediate oxides containing both 2+ and 4+ oxidation states (23−25). The reason is that, SnO can decompose according to the disproportionation reaction: $2SnO \rightarrow \beta\text{-}Sn + SnO_2$, even in the absence of oxygen at suitable temperature (1, 9). And

* Corresponding author. E-mail: h_cao@nimte.ac.cn.
Received for review November 28, 2009 and accepted March 08, 2010
[†] Chinese Academy of Sciences.
[‡] University of Michigan.
DOI: 10.1021/am900838z
2010 American Chemical Society

Published on Web 03/22/2010

thus, deposition ambient and growth temperature are of great importance in the fabrication of single phase SnO films.

In the present work, single-phase polycrystalline SnO thin films were fabricated on quartz by a two-step method, i.e., e-beam evaporation from high-purity SnO_2 source first and a subsequent vacuum annealing. The morphology, crystal phase, chemical composition, optical, and electrical properties of the obtained SnO thin films were characterized by or by using atomic force microscopy (AFM), X-ray diffraction (XRD), X-ray photoelectron spectroscopy (XPS), UV−vis−IR spectroscopy, photoluminescence (PL) spectroscopy, and Hall effect measurement, as detailed below.

EXPERIMENTAL METHODS

Before being put into the e-beam evaporation UHV system, quartz wafers were cleaned by organic solvents (alcohol and acetone), deionized H_2O, and subsequently dried in N_2 gas flow. After evacuating to 5.0×10^{-6} Pa, SnO_x (The subscript x stands for the unidentified phase) thin films were evaporated on quartz wafers from a high-purity SnO_2 source at room temperature (RT). The nominal film thickness and the deposition rate were around 250 and 2.5 nm/min, respectively. The film thickness was monitored by a quartz crystal oscillator which was formerly calibrated with α-step stylus profiler. Then the films were subjected to thermal annealing at 600 °C for 30 min (the optimum condition) in a vacuum chamber with base pressure of 2.0×10^{-4} Pa.

The surface morphologies of the samples were observed by using atomic force microscopy (AFM, Veeco Dimention V). XRD patterns were obtained in θ-2θ mode by using a multipurpose X-ray diffractometer (Bruker, D8 Advance) working with Cu-$K_\alpha$radiation. The phase composition of the SnO_x thin films was analyzed on an Axis Ultra X-ray photoelectron spectroscopy (XPS, Kratos Analytical Ltd., UK) equipped with a standard monochromatic Al-K_α source($h\nu = 1486.6$ eV). The binding energy data were calibrated with respect to the C1s signal of ambient hydrocarbons (C−H and C−C) at 284.8 eV. Transmittance and reflectance spectra were recorded via a UV−vis−IR spectrophotometer (Perkin-Elmer, Lambda 950) equipped with an integrating sphere, using $BaSO_4$ as reference. PL measurements were performed by using a 30 mW He−Cd laser for ultraviolet excitation ($\lambda = 325$ nm). Electrical properties were examined by Hall effect measurement system (ACCENT, HL5500). All measurements were performed at room temperature.

RESULTS AND DISCUSSION

As shown in Figure 1a, no extra peak was observed for the as-deposited SnO_x sample except the strong background, which indicates that the film is either amorphous or nanocrystalline (grain size less than 5 nm) in nature. For the annealed one (Figure 1b), all the diffraction peaks can be indexed to α-SnO phase with lattice constants of a = 3.802 Å and c = 4.836 Å (*P4/nmm*, JCPDS card 06−0395), implying that the annealed SnO film has polycrystalline structure without preferred orientation. Based on the analysis of ⟨101⟩ peak by using Scherrer formula, the average crystallite size is about 55 nm, which is in agreement with both the AFM images from this paper and earlier report (10). No characteristic peaks of impurities, such as elemental Sn or other tin oxide phases, were observed, indicating that the level of impurity is lower than the resolution limit of XRD (~5 at %).

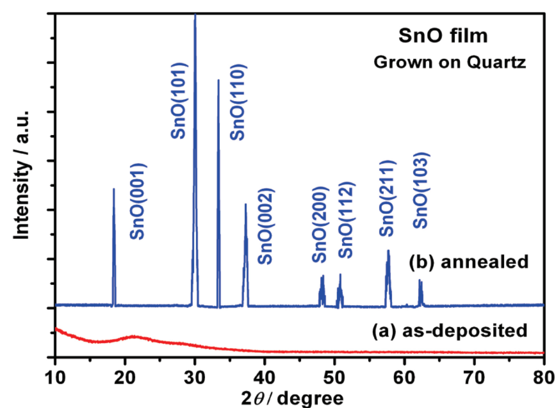

FIGURE 1. XRD patterns of the SnO_x samples on quartz: (a) as-deposited, (b) annealed.

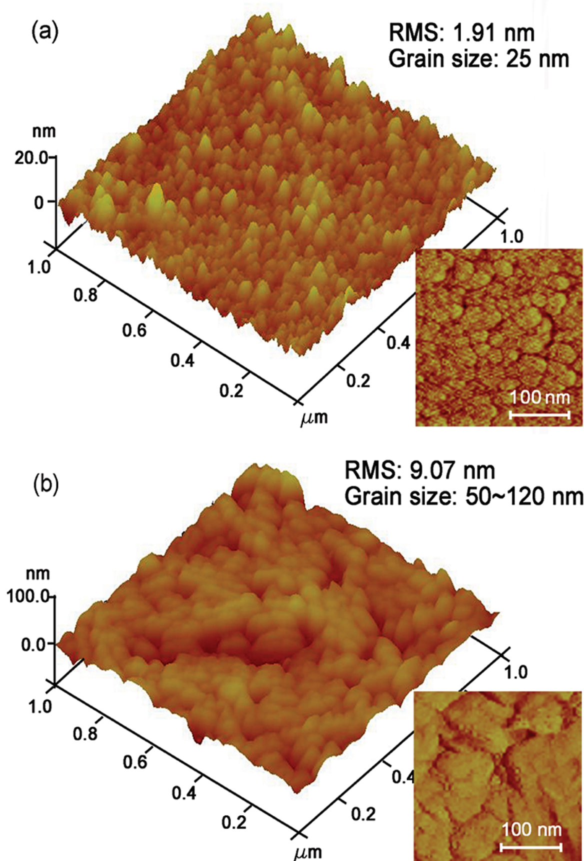

FIGURE 2. AFM morphologies of the SnO_x samples grown on quartz with a scan area of 1 μm × 1 μm (a) as-deposited, (b) annealed. The inset is the phase image.

Besides, it should be noted that the phase structure of the acquired samples was stable at different annealing temperatures, whereas higher deposition rate or/and longer annealing duration would lead to the emergence of β-Sn and SnO_2 phase (seen in the Supporting Information, Figure S1 and S2), which might result from the disproportionation of SnO phase.

Figure 2 shows the surface morphologies of the as-deposited and the annealed SnO_x thin films grown on quartz. Small grains with a mean size of ~25 nm (extracted from the phase images, seen in the inset of Figure 2a) are uniformly distributed on the film surface of the as-deposited

sample. However, it is clearly visible that ellipsoid-shaped grains with grain size of 50−120 nm (the inset of Figure 2b) are fused together compactly to form valleys and peaks along the annealed SnO_x film surface. Root-mean-square (rms) roughness of the as-deposited and the annealed SnO_x thin films is 1.91 and 9.07 nm, respectively. Those significant changes in grain shape and grain size can be attributed to the enhanced atom rediffusion and migration during annealing process, in which crystal grains grow along low stress directions, resulting in faceted surface and larger rms roughness. Moreover, this morphology is slightly different from its counterparts grown on α-sapphire (15), suggesting that the deposition methods and lattice mismatch between the film and the substrates ultimately determined the microstructure and surface morphology. It should be noted that determination of grain size by using AFM might be somewhat imprecise, because it can only detect the signal from the surface, and the observed inclusions can be consisted with aggregates rather than bulk grains.

Because the SnO_x films had been exposed to ambient air for an extended period, the surface layer could be oxidized before being introduced into the spectrometer (the reaction from SnO to SnO_2 is spontaneous in air based on the standard Gibbs energy of formation). To obtain the actual chemical composition of the SnO_x samples, we used high doses of argon ions (Ion energy of 2 KeV, current density of 5 μA/cm^2 roughly) to sputter away the top air-oxidized SnO_2 layer, the carbon contamination, as well as the hydrated layer. Figure 3 exhibits the XPS spectra of the fresh surfaces of two SnO_x samples and the air-oxidized SnO_2 surface layer of the as-deposited sample, in which the last one is taken as a reference (the spectra are thus comparable). As seen from the survey scan spectra in Figure 3, only Sn and O elements were observed except for a very small amount of C due to air contact. Regarding the air-oxidized SnO_2 layer, the dominant signals corresponding to Sn $3d_{5/2}$, Sn $3d_{3/2}$ were found at 486.6 eV, 495.0 eV (Figure 3c), matching very well with those reported for SnO_2 (26), and the other two peaks at 485.6 eV and 494.0 can be assigned to SnO (27). As for O 1s, the O 1s peak at 529.7 eV could be assigned to O in SnO and 530.4 eV for O in SnO_2 (26). Besides, the extra peak of O 1s at 531.9 eV can be indexed to −OH groups, which is thought to stem from the hydrated water. The peak deconvolution of both Sn 3d and O1s suggests that the coexistence of SnO and SnO_2 in the air-oxidized SnO_2 layer. Quantification gave the atomic ratio of Sn and O elements as 35.4/64.6 based on the areas of the Sn and O peaks within the experimental error, also indicating the existence of residual SnO in the air-oxidized SnO_2 layer.

After Ar^+ ion etching with diverse duration, the Sn 3d core levels and O 1s between two SnO_x samples are similar. The main band of Sn core levels $3d_{5/2}$ and $3d_{3/2}$ were observed at 485.6 and 494.0 eV, and the dominant bonding peak for O 1s is located at 529.7 eV, all in agreement with the reported value for SnO (27). In addition, two marginal component peaks at the Sn 3d spectra were also observed, i.e., metallic Sn and SnO_2, which is probably formed by the

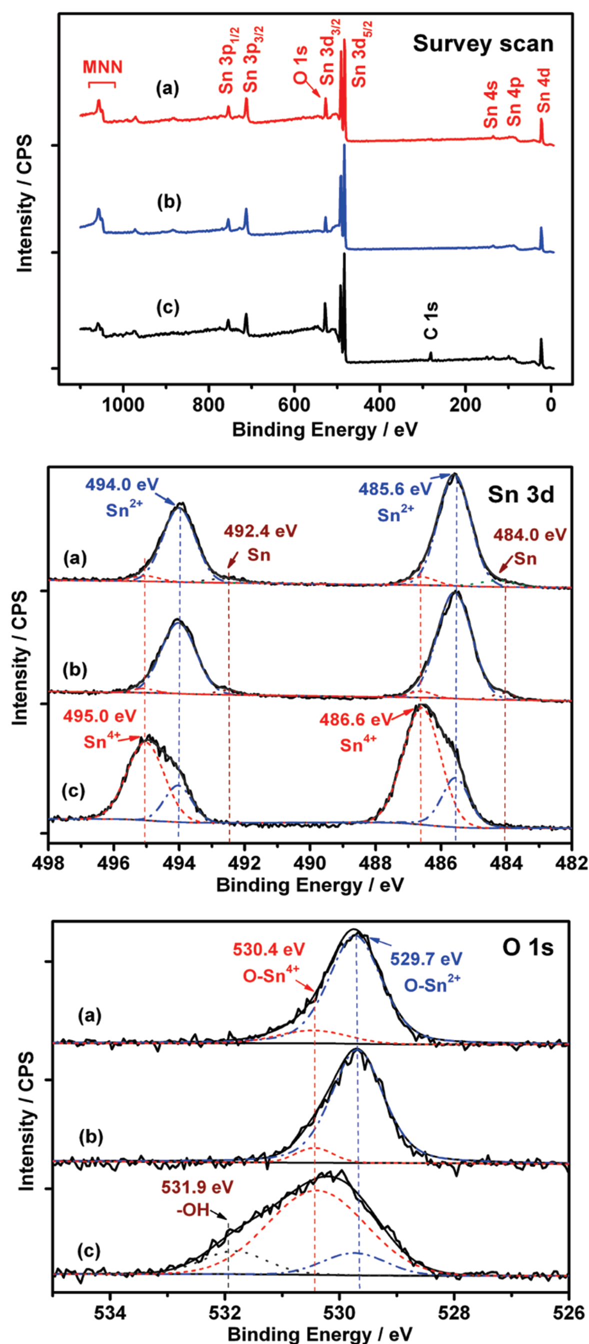

FIGURE 3. The survey scan, Sn 3d and O 1s core level XPS spectra of SnO_x samples: (a) as-deposited and after etching, (b) annealed and after etching, (c) air-oxidized SnO_2 layer as reference. The spectra have been normalized to equal height. The irregular lines stand for the raw data, and the smooth lines are the result of a curve fitting into various components.

ion etching of SnO, as previously described by Themlin et al. (28, 29). Concerning O 1s, no similar band of absorbed oxygen-containing species was observed after Ar^+ ion etching, suggesting the complete removal of the top hydrated layer. The main band is associated with the lattice oxygen from the SnO structure, while the shoulder at higher energies accounts for O−Sn^{4+} species, which is also ascribed to the Ar^+ ion etching, in line with the Sn 3d signals. The [Sn]/[O] ratios were determined to be 49.5/50.5 for the as-deposited sample and 49.7/50.3 for the annealed, all close to the ideal

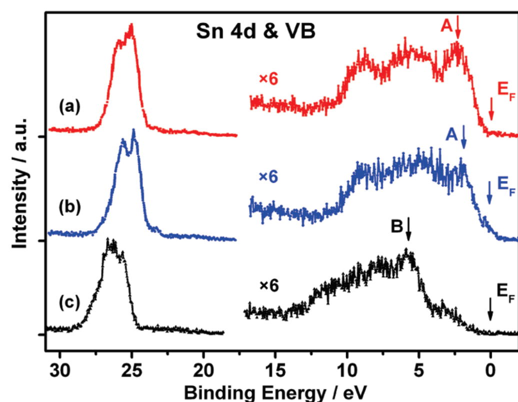

FIGURE 4. Photoelectron spectra of the Sn 4d core level and the valence band of SnO_x thin films: (a) as-deposited, (b) annealed, (c) air-oxidized SnO_2 layer. The VB region has been magnified with respect to the Sn 4d region on which the data have been normalized.

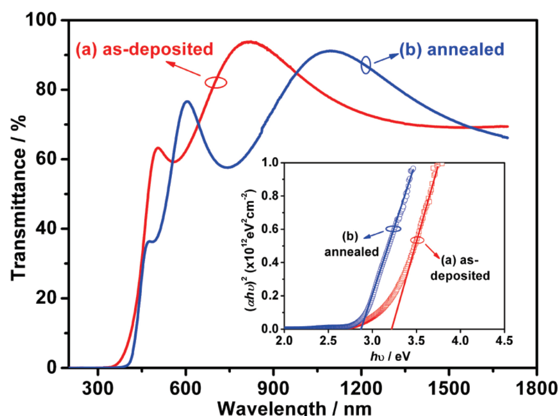

FIGURE 5. Optical transmittance spectra of the as-deposited and the annealed SnO samples in the range of 300−1700 nm. The inset shows $(\alpha h\nu)^2$ vs photon energy ($h\nu$) spectra for the two samples, where α is the absorption coefficient.

stoichiometric ratio of SnO. Consequently, the two SnO_x sample could be indentified as single phase SnO on the basis of XRD and XPS results. Moreover, as far as the air-oxidized SnO_2 layer is concerned, it will also necessitate the packaging and surface passivation for the optoelectronic and electronic applications.

For further evidence, the XPS spectra of the valence band (VB) and the Sn 4d core level are presented for the air-oxidized SnO_2 layer and two etched SnO_x samples. As shown in Figure 4, the most notable difference between two etched SnO_x samples and the SnO_2 layer is the presence of a prominent peak characteristic of SnO (labeled with A), at the low-energy side of the VB. This additional state at the VBM is attributed to long pair Sn 5s states (28, 29), as confirmed by density of states calculations (30). In addition, the Fermi levels (marked with E_F) is very close to the VBM of SnO, whereas for the air-oxidized SnO_2 layer, the energy band gap (labeled with B) is observed below E_F, which supports the p-type electronic structure in SnO film and n-type one in SnO_2 (17). Moreover, the closing of the band gap and the associated increase in the separation between the valence band leading edge (A and B) and the Sn 4d core level are also clearly observed, i.e., 23.6 eV for two etched SnO_x samples and 21.3 eV for the air-oxidized SnO_2 layer, in accordance with previous report (31). This increase in energy separation for SnO is mainly due to the smaller band gap of SnO compared to SnO_2.

The formation of SnO can be easily explained by assuming the following equilibrium at the surface of the crystallites: $2SnO_2 \rightleftharpoons 2SnO + O_2(g)$. In high vacuum conditions, the reaction production $O_2(g)$ was pumped out immediately, which shifts the equilibrium to the right and leads to the formation of SnO. This process is also understandable from the lattice structure point of view. In the SnO_2 rutile structure, each Sn atom has six oxygen neighbors, which forms a distorted octahedral with Sn−O nearest neighbor distance of 0.206 nm. In SnO, each Sn atom has four oxygen neighbors which located on the same side of the Sn atoms. The Sn−O bands have a length of 0.222 nm. Accordingly, the SnO_2 phase can be easily transformed into the SnO phase by removing the O atoms from SnO_2 and slightly adjusting the position of the Sn atoms (32). As for the disproportionation of SnO, it has been reported that SnO is metastable and decomposes into Sn and SnO_2 in vacuum at annealing temperature above 300 °C with noticeable rate (33, 34). However, all of those treatments were conducted on SnO powder samples, it is speculated that the relative smaller surface area is the reason for the thermal stability of SnO thin films in the present work.

Both SnO thin films have a yellowish color with an average optical transmittance of 70% in the wavelength range from 300 to 1700 nm, as shown in the Figure 5. The difference, though, is that the as-deposited SnO film exhibits a maximum transmittance value of about 93%, whereas the other shows a lower value of 91%, which is ascribed to the scattering light loss caused by the rough surface. Additionally, the absorption coefficient can be calculated from the following equation (35): $T = ((1 - R)^2 e^{-\alpha t})/(1 - R^2 e^{-2\alpha t})$, where R is the reflectance, t the film thickness. The optical measurement results were used to calculate the optical band gap (E_g) using Tauc's plot, which consists of extrapolating the linear part of $(\alpha h\nu)^2$ curves to zero. As seen in the inset of Figure 5, the E_g for the as-deposited and the annealed SnO thin films are estimated to be ~2.77 and 3.20 eV (with uncertainties 0.02 eV obtained from 5 repeated experiments and regression analysis), close to the reported band gap of tetragonal SnO (2.5−3.4 eV) (1, 14, 15). Previous studies indicate that the optical properties near the absorption edge are strongly influenced by the quality of films, which combined many factors including chemical composition, crystalline size, and the amount of structural defects (19, 36). In this case, the chemical composition in those samples does not change much. Also, because the reduction of structural defects caused by annealing process would lead to the decrease of band tail states and the blue-shift of the band gap, this redshift of band gap after annealing could be attributed to the crystalline size related quantum size effects, as reported on several different systems including CdS (37) and SnO_2 (38, 39). According to Brus model, when the grain size is comparable to or below the exciton Bohr radius, the energy difference ΔE_g between the nanocrystalline semi-

ARTICLE

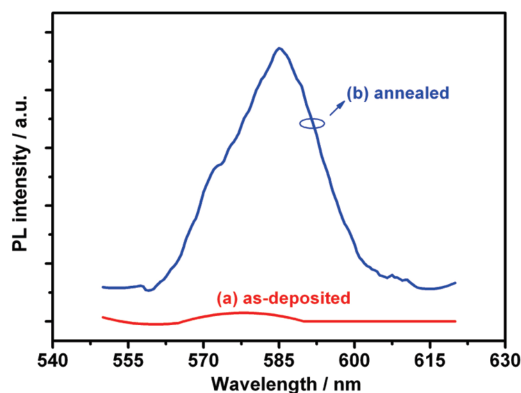

FIGURE 6. PL spectra for SnO thin films on quartz, (a) as-deposited, (b) annealed.

conductor band gap and the bulk energy gap versus crystalline radius R can be represented as (37, 40)

$$\Delta E_g(R) = E_g(R) - E_g(R \rightarrow \infty) = \frac{\hbar^2\pi^2}{2R^2}\left(\frac{1}{m_e^*} + \frac{1}{m_h^*}\right) \quad (1)$$

where the correction term was neglected, E_g ($R \rightarrow \infty$) is the bulk energy gap, and m_e^* and m_h^* (= $2.05m_e$ in SnO (17), m_e the mass of rest electron) are the effective masses of electrons and holes, respectively. However, the electron effective mass of SnO is not available, so $m_e^* = 0.27m_e$ of SnO_2 was taken into calculation tentatively (38). Assuming the mean grain sizes of 5 nm for the as-deposited sample and 55 nm after annealing, a notable redshift as much as 0.54 eV was obtained, which is even bigger than the experimental value in the present work (0.43 eV). Taking both the grain size and electron effective mass into account, it is entirely possible that the increase in grain size could be responsible for the discrepancy of the optical band gaps between the as-deposited and the annealed SnO thin films.

Moreover, the PL spectra of the as-deposited and the annealed SnO thin films were measured at RT using a He−Cd laser (λ = 325 nm), as displayed in Figure 6. Unfortunately, no intrinsic optical transition luminescence, except a weak yellow emission at 585 nm was observed in the spectrum for the annealed sample. These PL properties are very similar to SnO_2 nanorods which prepared by solution synthesis (41) or SnO_2 nanoribbons by laser ablation (42). In those works, the luminescence centers around 580 nm were generally assigned to crystal defects or defect levels associated with oxygen vacancies, or tin interstitials that have formed during growth process (41). In addition, it is noticed that specific treatment like outgassing or vacuum at temperatures exceeding 300−400 °C can remove surface framework oxygen atoms and lead to the formation of surface oxygen vacancies: $V_O^{\bullet\bullet}$, $V_O^{\bullet}$, and V_O (25, 43). Likewise, in our case of SnO, we suspect that the formation of nonstoichiometric SnO is not accompanied by the formation of oxygen vacancies at the surface of the solid, whereas the vacuum annealing process leads to the removal of surface framework oxygen atoms and the formation of surface oxygen vacancies, and those oxygen vacancies finally result in the yellow emission at 585 nm for the annealed sample. Meanwhile, the relatively lower surface area is also the reason for the weaker peak when compared with the yellow-emission peak in SnO_2 powder.

The electrical properties of the SnO thin films were studied by Hall effect measurement using a van der Pauw configuration, as seen in Table 1. Hall effect measurements indicated that the annealed SnO film shows a p-type behavior, with resistivity of 156 Ω cm, hole mobility (μ_h) of 1.4 $cm^2 V^{-1} s^{-1}$ and hole concentration (N_h) of 2.8×10^{16} cm^{-3}. However, the as-deposited film has a high resistivity of 4×10^4 Ω cm, which is beyond the measuring range of the Hall effect measurement. On the basis of first-principle calculations, Togo et al. suggested that the p-type conductivity of SnO films originated from the excess of oxygen or/and the tin vacancy (44, 45). Meanwhile, experimental results also verified the relation between the p-type conductivity and the degree of the off-stoichiometry in epitaxial SnO films (15). In the present case, both the as-deposited and the annealed SnO thin films have an excess of oxygen, in line with those above-mentioned reports. However, quantitatively analyzing, the less conductive as-deposited film ([Sn]/[O] = 49.5/50.5) has similar oxygen content with the annealed one ([Sn]/[O] = 49.7/50.3), according to the chemical composition determined by XPS. This discrepancy in conductivity can be interpreted by the improvement of film quality. During the vacuum annealing process, an increase in grain size takes place, which reduces the carrier scattering from grain boundary, thereby giving rise to the improvement of carrier mobility and film conductivity. Particularly, the value of hole concentration is nearly an order of magnitude lower than those reported by Ogo et al. (14), which might lead to larger field effect mobility and make it more suitable for p-type TFT application.

Table 1. Hall Effect Parameters of Available SnO Films

substrate	deposited method	resistivity (Ω cm)	carrier type	N_h (cm^3)	μ_h ($cm^2 V^{-1} s^{-1}$)	ref
quartz	EB, as-deposited	4×10^4				present work
quartz	EB, annealed at 600 °C	156	p	2.8×10^{16}	1.4	present work
α-sapphire	EB, annealed at 600 °C	58	p	5.6×10^{16}	1.9	present work[a]
α-sapphire	EB, as-deposited	195	p			Pan et al.(15)
yttria-stabilized zirconia (YSZ)	PLD	10.4	p	2.5×10^{17}	2.4	Ogo et al.(14, 17)

[a] Sample deposited on α-sapphire at the same batch.

CONCLUSIONS

In summary, SnO thin films have been synthesized from routine semiconductor processes based on e-beam evaporator and vacuum annealing facility, with a character of large area, ease in operation and scale up, and low thermal budget with respect to in situ high temperature deposition method. The as-deposited amorphous or nanocrystalline SnO was converted to polycrystalline SnO phase after optimum vacuum annealing condition. The SnO_x samples could be indentified as single phase SnO, because the [Sn]/[O] ratios of the fresh surface were obtained to be 49.5/50.5 for the as-deposited sample and 49.7/50.3 for the annealed one, all close to the ideal stoichiometric ratio of SnO. The formation mechanism of SnO thin films was presented on the basis of both thermodynamics of reactions and atomic configuration in the crystal structures. The optical bandgap of the as-deposited and the annealed SnO thin films was determined to be 2.77 and 3.20 eV, respectively, and the optical band gap difference was interpreted tentatively based on Brus's model. No near band edge emission, but only a weak peak at 585 nm was observed in PL spectrum at room temperature. Moreover, the obtained film exhibited a hole mobility of 1.4 $cm^2 V^{-1} s^{-1}$ and a hole density (N_h) of 2.8×10^{16} cm^{-3}. In this article, we suggest that the reasonable optical, electrical properties of SnO film and the easy preparation process make it suitable for optoelectronic and electronic device applications.

Acknowledgment. The authors acknowledge the help of De-Chun Liang in the Institute of Semiconductors, CAS, for collecting the PL data. This work was financial supported by the key project of the Natural Science Foundation of Zhejiang province, P. R. China (Grant 0804201051), and the Special Foundation of President of Chinese Academy of Sciences (Grant 080421WA01).

Supporting Information Available: XRD pattern of the annealed SnO sample with different annealing temperature: as-deposited, 300 °C annealed, 400 °C annealed, 500 °C annealed, 650 °C annealed (Figure S1); XRD pattern of the annealed SnO sample with deposition rate 10 nm/min, the annealing temperature and duration was 600 °C and 30 min, respectively (Figure S2) (PDF). This material is available free of charge via the Internet at http://pubs.acs.org.

REFERENCES AND NOTES

(1) Blanca, E. L. P. Y.; Svane, A.; Christensen, N. E.; Rodriguez, C. O.; Cappannini, O. M.; Moreno, M. S. *Phys. Rev. B* **1993**, *48*, 15712.
(2) Watson, J. *Sens. Actuators* **1984**, *5*, 29.
(3) Hara, K.; Horiguchi, T.; Kinoshita, T.; Sayama, K.; Sugihara, H.; Arakawa, H. *Sol. Energy Mater. Sol. Cells* **2000**, *64*, 115.
(4) Zhang, Q. H.; Saraf, L. V.; Hua, F. *Nanotechnology* **2007**, *18*, 195204.
(5) Calderer, J.; Molinas, P.; Sueiras, J.; Llobet, E.; Vilanova, X.; Correig, X.; Masana, F.; Rodriguez, A. *Microelectron. Reliab.* **2000**, *40*, 807.
(6) Odani, A.; Nimberger, A.; Markovsky, B.; Sominski, E.; Levi, E.; Kumar, V. G.; Motiei, A.; Gedanken, A.; Dan, P.; Aurbach, D. *J. Power Sources* **2003**, *119*, 517.
(7) Han, Z. H.; Guo, N.; Li, F. Q.; Zhang, W. Q.; Zhao, H. Q.; Qian, Y. T. *Mater. Lett.* **2001**, *48*, 99.
(8) Qiang, Z.; Richard, A. B. *J. Appl. Polym. Sci.* **1995**, *57*, 1465.
(9) Fan, H. Y.; Reid, S. A. *Chem. Mater.* **2003**, *15*, 564.
(10) Pan, X. Q.; Fu, L. *J. Appl. Phys.* **2001**, *89*, 6048.
(11) Kim, K. K.; Kim, H. S.; Hwang, K. K.; Lim, J. H.; Park, S. J. *Appl. Phys. Lett.* **2003**, *83*, 63.
(12) Bosman, A. J.; Crevecoeur, C. *Phys. Rev.* **1966**, *144*, 763.
(13) Pollack, G. P.; Trivich, D. *J. Appl. Phys.* **1975**, *46*, 163.
(14) Ogo, Y.; Hiramatsu, H.; Nomura, K.; Yanagi, H.; Kamiya, T.; Hirano, M.; Hosono, H. *Appl. Phys. Lett.* **2008**, *93*, 32113.
(15) Pan, X. Q.; Fu, L. *J. Electroceram.* **2001**, *7*, 35.
(16) Guo, W; Fu, L.; Zhang, Y.; Graham, G.; Pan, X. Q.; Liang, L. Y.; Liu, Z. M.; Cao, H. T. *Appl. Phys. Lett.* **2010**, *96*, 042113.
(17) Ogo, Y.; Hiramatsu, H.; Nomura, K.; Yanagi, H.; Kamiya, T.; Kimura, M.; Hirano, M.; Hosono, H. *Phys. Status Solidi, A* **2009**, *206*, 2187.
(18) Srikant, V.; Clarke, D. R. *J. Appl. Phys.* **1997**, *81*, 6357.
(19) Sivaramasubramaniam, R.; Muhamad, M. R.; Radhakrishna, S. *Phys. Status Solidi, A* **1993**, *136*, 215.
(20) Domashevskaya, E. P.; Chuvenkova, O. A.; Kashkarov, V. M.; Kushev, S. B.; Ryabtsev, S. V.; Turishchev, S. Y.; Yurakov, Y. A. *Surf. Interface Anal.* **2006**, *38*, 514.
(21) Goldsmith, S.; Cetinorgu, E.; Boxman, R. L. *Thin Solid Films* **2009**, *517*, 5146.
(22) Lin, J. M.; Cheng, C. L.; Lin, H. Y. *Opt. Lett.* **2006**, *31*, 3173.
(23) Krasevec, V.; Skraba, Z.; Hudomalj, M.; Sulcic, S. *Thin Solid Films* **1985**, *129*, L61.
(24) Song, P. X.; Wen, D. S. *J. Phys. Chem. C.* **2009**, *113*, 13470.
(25) Popescu, D. A.; Herrmann, J. M.; Ensuque, A.; Verduraz, F. B. *Phys. Chem. Chem. Phys.* **2001**, *3*, 2522.
(26) Her, Y. C.; Wu, J. Y.; Lin, Y. R.; Tsai, S. Y. *Appl. Phys. Lett.* **2006**, *89*, 043115.
(27) Ahn, H. J.; Choi, H. C.; Park, K. W.; Kim, S. B.; Sung, Y. E. *J. Phys. Chem. B.* **2004**, *108*, 9815.
(28) Kover, L.; Kovacs, Z.; Sanjines, R.; Moretti, G.; Cserny, I.; Margaritondo, G.; Palinkas, J.; Adachi, H. *Surf. Interface Anal.* **1995**, *23*, 461.
(29) Themlin, J. M.; Chtaib, M.; Henrard, L.; Lambin, P.; Darville, J.; Gilles, J. M. *Phys. Rev. B* **1992**, *46*, 2460.
(30) Themlin, J. M.; Sporken, R.; Darville, J.; Caudano, R.; Gilles, J. M.; Johnson, R. L. *Phys. Rev.B* **1990**, *42*, 11914.
(31) Batzill, M.; Diebold, U. *Prog. Surf. Sci.* **2005**, *79*, 47.
(32) Maestre, D.; Ramirez-Castellanos, J.; Hidalgo, P.; Cremades, A.; Gonzalez-Calbet, J. M.; Piqueras, J. *Eur. J. Inorg. Chem.* **2007**, *11*, 1544.
(33) Giefers, H.; Porsch, F.; Wortmann, G. *Solid State Ionics.* **2005**, *176*, 199–207.
(34) Moreno, M. S.; Punte, G.; Rigotti, G.; Mercader, R. C.; Weisz, A. D.; Blesa, M. A. *Solid State Ionics* **2001**, *144*, 81.
(35) Youssef, S.; Combette, P.; Podlecki, J.; Al Asmar, R.; Foucaran, A. *Cryst. Growth Des.* **2009**, *9*, 1088.
(36) Cabot, A.; Arbiol, J.; Ferre, R.; Morante, J. R.; Fanglin, C.; Meilin, L. *J. Appl. Phys.* **2004**, *95*, 2178.
(37) Brus, L. E. *J. Chem. Phys.* **1984**, *80*, 4403.
(38) Lee, E. J. H.; Ribeiro, C.; Giraldi, T. R.; Longo, E.; Leite, E. R.; Varela, J. A. *Appl. Phys. Lett.* **2004**, *84*, 1745.
(39) Yuan, Z. Z.; Li, D. S.; Wang, M. H.; Chen, P. L.; Gong, D. R.; Cheng, P. H.; Yang, D. R. *Appl. Phys. Lett.* **2008**, *92*, 121908.
(40) Castillo, D. J.; Rodriguez, V. D.; Yanes, A. C.; Ramos, J. M.; Torres, M. E. *Nanotechology* **2005**, *16*, S300.
(41) Cheng, B.; Russell, J. M.; Shi, W. S.; Zhang, L.; Samulski, E. T. J. *J. Am. Chem. Soc.* **2004**, *126*, 5972.
(42) Hu, J. Q.; Bando, Y.; Liu, Q. L.; Golberg, D. *Adv. Funct. Mater.* **2003**, *13*, 493.
(43) Sergent, N.; Gelin, P.; Perier-Camby, L.; Praliaud, H.; Thomas, G. *Sens. Actuators, B* **2002**, *84*, 176.
(44) Moreno, M. S.; Varela, A.; OteroDiaz, L. C. *Phys. Rev. B* **1997**, *56*, 5186.
(45) Togo, A.; Oba, F.; Tanaka, I.; Tatsumi, K. *Phys. Rev. B* **2006**, *74*, 195128.

AM900838Z

ARTICLE